PCCP

Mechanism of Creation and Destruction of Oxygen Interstitial Atoms by Nonpolar Zinc Oxide(10\bar{1}0) Surfaces

Journal:	*Physical Chemistry Chemical Physics*
Manuscript ID	CP-ART-03-2021-001204.R1
Article Type:	Paper
Date Submitted by the Author:	22-Jun-2021

Complete List of Authors:	Jeong, Heonjae; University of Illinois, Department of Mechanical Science and Engineering Li, Ming; University of Illinois at Urbana-Champaign Kuang, Jingtian; University of Illinois at Urbana-Champaign Ertekin, Elif; University of Illinois, Department of Mechanical Science and Engineering Seebauer, Edmund; University of Illinois, Chemical & Biomolecular Engineering

Mechanism of Creation and Destruction of Oxygen Interstitial Atoms by Nonpolar Zinc Oxide($10\bar{1}0$) Surfaces

Heonjae Jeong[a], Ming Li[b], Jingtian Kuang[b], Elif Ertekin[a], and Edmund G. Seebauer*[b]

[a]Department of Mechanical Science and Engineering, University of Illinois at Urbana-Champaign, Urbana, Illinois 61801, USA

[b]Department of Chemical and Biomolecular Engineering, University of Illinois at Urbana-Champaign, Urbana, Illinois 61801, USA

*Corresponding author: Edmund G. Seebauer

Abstract

Oxygen vacancies (V_O) influence many properties of ZnO in semiconductor devices, yet synthesis methods leave behind variable and unpredictable V_O concentrations. Oxygen interstitials (O_i) move far more rapidly, so post-synthesis introduction of O_i to control the V_O concentration would be desirable. Free surfaces offer such an introduction mechanism if they are free of poisoning foreign adsorbates. Here, isotopic exchange experiments between nonpolar ZnO($10\bar{1}0$) and O_2 gas, together with mesoscale modeling and first-principles calculations, point to an activation barrier for injection only 0.1–0.2 eV higher than for bulk site hopping. The modest barrier for hopping in turn enables diffusion lengths of tens to hundreds of nanometers only slightly above room temperature, which should facilitate defect engineering under very modest conditions. In addition, low hopping barriers coupled with statistical considerations lead to important qualitative manifestations in diffusion via an interstitialcy mechanism that do not occur for vacancies.

Introduction

Oxygen vacancies (V_O) influence a variety of technologically relevant aspects of ZnO's behavior, including parasitic green emission in ultraviolet emitters,[1] carrier recombination rates in photocatalysts,[2] ferromagnetism in spintronics,[3–5] piezoelectricity in nanogenerators,[6] and free electron density in p-n junctions.[7] ZnO synthesis methods leave behind variable and unpredictable concentrations of V_O. Oxygen interstitials (O_i) are more thermodynamically stable in ZnO under O-rich conditions,[8–11] so post-synthesis introduction of O_i under such conditions to eliminate V_O or adjust its concentration would be desirable. The barrier for O_i hopping lies well below that for V_O,[8,12–15] suggesting surfaces as the venue for such introduction. Indeed, single-crystal isotopic labeling experiments examining different crystallographic orientations[16] and the effects of foreign adsorbates[17] show that suitably prepared surfaces offer an efficient pathway for introduction that changes the primary O-related point defect from V_O. The magnitudes of measured diffusivities and their temperature dependence[16,17] together with crystal color changes[16] have confirmed O_i as the species that controls V_O.

Those diffusion experiments involved *c*-axis polar surfaces of the wurtzite structure – both O-term ($000\bar{1}$) and Zn-term (0001). The polarity leads to complicated reconstructions,[18–22] creating experimental and computational challenges for identifying the active sites for O_i injection. To mitigate those complications, the present work uses similar experimental methods for nonpolar ZnO($10\bar{1}0$) that does not reconstruct, together with first-principles calculations interpreted in light of mesoscale models. The models highlight important qualitative manifestations of diffusion via an interstitialcy mechanism that do not occur for vacancies. These manifestations arise from the low barriers for interstitial diffusion and statistical effects.

The present results enable direct comparison among polar and nonpolar ZnO surfaces, and to behavior of related oxide surfaces such as nonpolar rutile TiO_2(110), whose role in O_i creation and destruction is understood in considerable detail.[23] Despite differing mechanisms by which O_i exchanges with nonpolar surfaces, they exhibit injection barriers only 0.1-0.2 eV higher than for bulk site hopping. The hopping barriers themselves for O_i lie below 1 eV, and enable diffusion lengths of tens to hundreds of nanometers or more only slightly above room temperature. Such high rates of diffusion could facilitate defect engineering under very modest conditions.

Methods

1. Experiment

A well-known isotopic gas-solid self-diffusion method was employed[24–26] to monitor the diffusional behavior of O defects indirectly. The technique begins with extended exposure of the solid having natural-abundance isotope concentrations to O_2 at a selected temperature and pressure to attain steady-state populations of defects, typically assumed to equal the equilibrium concentrations.[25,26] The gas is then abruptly switched to the isotopically labeled form. After temperature quenching at the desired diffusion time, the isotopic profile is measured with *ex-situ* time-of-flight secondary ion mass spectrometry (SIMS).

Wurtzite nonpolar $(10\bar{1}0)$-terminated ZnO single-crystal specimens (10 mm × 5 mm × 0.5 mm, CrysTec GmbH) with minimal roughness (< 5 Å) were employed. Prior to mounting, the specimens were degreased by successive 5 min ultrasonic baths in acetone, isopropanol, and methanol. The specimens were mounted in an ultrahigh vacuum (UHV) chamber that was turbomolecularly pumped. The base pressure for the UHV chamber was below 10^{-7} Torr. Type K

(chromel-alumel) thermocouples were spring-loaded against the center of each specimen to monitor the surface temperature. Pre-annealing in natural abundance O_2 gas (S. J. Smith Co., $\geq$ 99.995%) was performed for 6 hr at the diffusion temperature T and oxygen pressure P_{O_2} to desorb surface contaminants and to equilibrate the defect concentrations. The specimens were subsequently annealed in isotopic $^{18}O_2$ gas (Sigma-Aldrich, $\geq$ 99%) for 105 min at T = 510 – 600 °C and P_{O_2}= 10^{-5} – 10^{-4} Torr. Measurements of the ^{18}O concentration profiles by SIMS employed a PHI-TRIFT III instrument with a Cs ion beam source operating at 3 keV, with baseline concentrations checked against known isotopic fractions. *Ex situ* measurements by X-ray photoelectron spectroscopy (XPS) of selected surfaces after degreasing and after subsequent annealing or self-diffusion indicated no significant changes in surface composition or bonding state.

2. Atomic scale modeling

First-principles calculations by density functional theory (DFT)[27,28] employed the Vienna *Ab-Initio* Simulation Package (VASP)[29,30] with projector augmented wave (PAW)[31] pseudopotentials and the Perdew-Burke-Eznerhof (PBE)[32] exchange-correlation functional in the generalized gradient approximation (GGA).[32] A plane-wave energy cutoff of 530 eV was used, with a total energy convergence threshold of 10^{-6} eV. Brillouin zone sampling employed a 3 × 3 × 1 Monkhorst-Pack k-point mesh. A 15 Å vacuum region separated the surface from periodic images.

Following existing literature,[33,34] the ZnO($10\bar{1}0$) slab incorporated five Zn-O layers, with each layer incorporating a 2×2 arrangement of four repeated unit cells. Relaxation of the atomic positions in all five layers determined the surface geometry, which exposes three-fold coordinated Zn and O atoms in a 1:1 stochiometric ratio. Published literature has already

examined the geometry of adsorbed oxygen atoms on ZnO($10\bar{1}0$).[35–37] The pristine (*i.e.*, undefected) surface of ZnO($10\bar{1}0$) has the lowest surface energy of all orientations,[38] and O_2 adsorption is not energetically favorable. However, when oxygen vacancies or zinc-oxygen dimer vacancies are present, O_2 adsorbs dissociatively with a modest energy near 1.1 eV.[37] Under the O-rich conditions characterizing the present experiments, such vacancies are unlikely to be present in large quantities.[37] However, for the related nonpolar semiconducting oxide surface of rutile TiO_2(110), dissociative adsorption of O_2 occurs at step edges.[39] It is therefore plausible for ZnO($10\bar{1}0$) that O_2 also dissociates at step edges.

Furthermore, it is also plausible that the O atoms produced by dissociation diffuses onto terrace sites. Neither the surface diffusion barrier nor the energy needed to release O atoms from step edges to terraces is known for ZnO($10\bar{1}0$). However, temperature programmed desorption after exposure of this surface to O_2[40] yields a peak at 450K, which shifts upward to 500K with step edges corresponding to the mis-orientation (4($10\bar{1}0$)×(0001)). Desorption is more energetically costly, and therefore occurs at higher temperatures, than surface diffusion or release of edge-bound adsorbates onto nearby terraces. These desorption temperatures lie well below those used here, meaning that release of O atoms onto terraces should occur readily. The adsorbed O would bond in a geometry corresponding to that for O_2 adsorption at O vacancies,[35–37] and the present work adopted that geometry.

Minimum energy pathways and the corresponding activation barriers were computed using the climbing image nudged elastic band (CI-NEB) method.[41] With a spring constant of -5 eV Å^{-1}, atomic positions in each image were determined from linear interpolation between two local minimum energy states. The resulting geometries were relaxed until the maximum total force on any atom fell below 0.05 eV Å^{-1}.

The DFT-computed lattice constants of a = 3.288 Å, c = 5.303 Å, internal parameter u = 0.378 Å, and bandgap E_g = 0.59 eV, agree satisfactorily with previous DFT-GGA[42] values of a = 3.288, c = 5.305, u = 0.379, and E_g = 0.73 eV. The formation energy for O_i under maximally O-rich conditions of 1.4 eV for a $4 \times 4 \times 4$ bulk supercell lies close to the corresponding value of 1.3-1.4 eV in the deepest layers of the slab supercell, which implies that the number of layers in the slab is sufficiently large.

To allow for the possible creation of charged (acceptor) metastable states during formation of bulk O_i from adsorbed O, we 'doped' the slab by introducing an artificial O vacancy (V_O) at the back side according to methods described previously.[23,43] Even with the addition of V_O, bulk O_i and adsorbed O remains neutral, consistent with prior DFT results[8–11,44,45] that yield neutral O_i all values of the Fermi energy.

3. Mesoscale modeling

Quantitative interpretation of the experimental isotopic diffusion profiles, as well as connection to first principles calculations, requires mesoscale modeling over length scales ranging from roughly 2 to 500 nm. Several approaches exist. The findings of the present work rest primarily on a classical thermodynamic model and a microkinetic model. The classical model uses analytical profile-by-profile fitting to yield the net isotope injection flux F and the tracer diffusion coefficient D_{tr}. The microkinetic model numerically fits all the profiles simultaneously to yield a suite of elementary-step numerical parameters suitable for direct comparison with DFT.

Classical thermodynamic models for tracer diffusion assume global equilibrium throughout the solid.[46] (For "chemical" diffusion, where isotopic exposure coincides with a concurrent change in T or P_{O_2}, local equilibrium is assumed.[47,48]) Classical approaches quantify the profiles

through an analytical mathematical formulation in terms of quantities that represent composites of other parameters. For example, F incorporates the rate constants for O_i injection and annihilation, and the concentration $[O_i]$ of O_i in the near-surface bulk. Similarly, D_{tr} incorporates the hopping diffusivity D_{hop}, $[O_i]$, and (in the case of chemical diffusion) a thermodynamic factor. Most parameters within F and D_{tr} in turn comprise activation energies, pre-exponential factors, and other quantities.

Literature that incorporates surface participation into the analysis typically quantifies F in terms of a surface exchange coefficient K. This formulation expresses the phenomenological notion that the flux of isotopic label through the surface is proportional to the difference in isotopic mole fractions between the gas and the solid at the surface.[49–51] Expressed mathematically, the rate of isotope exchange obeys[52]

$$F = K(C_g - C_s) = -D_{tr}\frac{\partial C}{\partial x}\Big|_{x=0} \quad (1),$$

where C_g and C_s respectively denote the isotopic mole fraction in the gas and solid, and x is the spatial dimension. K is defined without reference to any particular microscopic mechanism.[50] K is sometimes believed[26,53,54] to incorporate only surface properties independent of the bulk diffusivity. For example, variations of K with temperature have been attributed to segregation of extrinsic elements to the surface.[52] However, it has been shown experimentally[55] and mathematically[56] that K depends upon the bulk diffusivity in some kinetic regimes. Accordingly, more recent treatments of F focus on the kinetics of the surface-defect interaction.[23,57] In this spirit, the present treatment uses F itself rather than K, so that profile fitting yields F and D_{tr}.

Representation of self-diffusion at a more detailed level suitable for mechanistic evaluation employs numerical simulators based on continuum diffusion equations[58,59] or Monte Carlo methods.[60,61] The simulators incorporate interactions of point defects with each other, extended

defects, electric fields, and nearby surfaces. Profile fitting yields activation energies, pre-exponential factors, and related parameters. Direct comparison with results from DFT becomes possible. However, the simulators necessarily assume specific functional forms for each mathematical expression describing the diffusion-reaction network – a challenging drawback when the identities of key species and their reaction kinetics remain poorly understood.

A complete microkinetic model employs not only a simulator but also an optimization algorithm that determines a set of elementary-step parameter to provide the best fit of an aggregated set of profiles.[57,62,63] Core features of the simulator and optimizer used here appear elsewhere.[23,57,62,64] The optimizer remained unchanged, employing a weighted sum of squared errors approach with an iteration tolerance of 1% in the objective function. However, the simulator was adapted from previous work to incorporate new expressions describing sequestration of O_i.

The Electronic Supplementary Information (ESI) supplies further background for these models and discusses more details of their implementation. The ESI also describes other mesoscale modeling approaches applied to the data set that did not bear as much fruit, but by their inadequacy proved to be useful points of reference for the models presented here.

4. Implementation of microkinetic model

Movement of ^{18}O from the gas into the solid entails adsorption of O_2, dissociation into adsorbed O, conversion into injectable form, and injection into the bulk solid. Microkinetic models treat only the solid-phase processes downstream of the conversion into injectable form; the coverage θ of injectable oxygen appears in the boundary conditions for the differential equations. No unified treatment yet exists that links the adsorption, dissociation and conversion processes to θ.

For example, the general relationship between θ and the total coverage of adsorbed O remains unknown. A recent first principles treatment[23] by DFT has resolved many aspects of that question for TiO_2(110), indicating that most (but not all) adsorbed oxygen resides in injectable form. With the assumption that O_2 adsorption and dissociation are rapid, independent knowledge of the gas adsorption isotherm would suffice to yield θ. However, that knowledge is typically difficult to obtain. Experimental determination requires coverage measurements pressures above the range of most electron or ion spectroscopies. Computational estimation of θ by DFT requires calculation of adsorption entropies that are seldom attempted.

Thus microkinetic modeling requires assumptions to estimate θ. Following previous literature,[23,57,62,64] we assume that [O_i] obeys a conventional thermodynamic equilibrium expression. A different approach detailed in the ESI exploits the weak dependence of the present profiles on T and P_{O_2}.

The microkinetic model retains many aspects of a similar model described elsewhere for ZnO(0001). [47] However, significant changes include incorporation of a statistical factor as described in the Discussion, a different charge state for O_i, and a different sequestration mechanism. The following paragraphs briefly describe the charge state and sequestration mechanism.

O_i in the ZnO bulk exists in charge states ranging from 0 to –2 depending upon the Fermi energy E_F.[9,12,65] Single-crystal ZnO typically manifests modestly n-type behavior, for which most DFT evidence points to a neutral dumbbell geometry.[8–11,44,45] The neutral charge state renders the formation energy ΔH_f for O_i independent of E_F.

The sequestration mechanism involves sites S whose identity remains unknown and unspecified, but could correspond to species such as hydrogen interstitials and/or zinc vacancies.

The model describes such species with a single set of average kinetic and thermodynamic parameters. The sites can exist in forms that are complexed (S_C) or uncomplexed (S_U) with O_i according to

$$[O_i] + [S_U] \underset{r_{diss}}{\overset{r_{asso}}{\rightleftharpoons}} [S_C] \quad (2).$$

The association rate r_{asso} for formation of the complex obeys

$$r_{asso} = k_{asso}[O_i][S_U] \quad (3),$$

where k_{asso} denotes a diffusion-limited constant given by

$$k_{asso} = 4\pi a D_{hop} \quad (4),$$

and a denotes the capture radius of the sequestration site. This capture radius can depends upon several factors,[66] but was set here to the hop length of 2×10^{-8} cm^{-3}. The dissociation rate obeys

$$r_{diss} = k_{diss}[S_C] \quad (5),$$

where the dissociation rate constant k_{diss} obeys

$$k_{diss} = A_{diss}\exp(-E_{diss}/k_B T) \quad (6).$$

E_{diss} and A_{diss} respectively denote the activation energy and pre-exponential factor for dissociation, and k_B denotes Boltzmann's constant.

The concentrations $[S_C]$ and $[S_U]$ sum to yield the total concentration of sequestration sites [S] according to

$$[S] = [S_C] + [S_U] \quad (7).$$

The concentration [S] may depend upon interaction with other species that do not complex with O_i and whose identities are unknown. The model therefor assumes [S] obeys a thermodynamic expression

$$[S] = S_{tot}\exp(-\Delta H_{fs}/k_B T)\left(\frac{P_{O_2}}{P^0}\right)^c \quad (8).$$

with ΔH_{fs} representing an effective standard enthalpy of formation and S_{tot} incorporating an effective standard formation entropy and related scaling constants. P_{O_2} is scaled to a reference pressure P^0 of 1 atm, and raised to a phenomenological power c. Since O_i bonds to S with significant affinity, it plausible that most S exists in complexed form such that $[S] \approx [S_C]$.

Results

1. ^{18}O isotopic concentration profiles

Figure 1(a) shows experimental diffusion profiles for ^{18}O in the ranges $T = 510 - 600$ °C and $P_{O_2} = 5 \times 10^{-5}$ Torr. The ^{18}O concentrations rise to about 1%, which is well above the natural-abundance baseline of 0.2%. As in related work for polar Zn-term ZnO(0001)[16,17] and O-term ZnO($000\bar{1}$)[16] surfaces, the profiles exhibit very shallow slopes down to depths of several hundred nanometers, beyond which SIMS measurements require impractically long times in the absence of cross sectional line scans[67] or powder techniques.[68] Such flat profiles characterize diffusion wherein surface processes constitutes the rate-limiting step rather than diffusion in the bulk.[56] Despite this challenge, the profiles in normalized form yield nonzero slopes of magnitudes appropriate for classical mesoscale modeling. Figure S1 in the ESI shows an example.

The profiles typically exhibit a small degree of ^{18}O pile-up within a few tens of nanometers of the surface. This phenomenon has been observed for other ZnO surfaces, particularly ZnO(0001), and originates from the interaction between surface band bending and the drift[69,70] and perhaps ionization state[71] of mobile O_i. The pile-up incorporates <1% of the total injected ^{18}O, however, and may be neglected during analysis of the profiles at greater depths.[69,72] Hence, the pile-up will not be discussed further here.

2. Atomic scale modeling

Figure 2 summarizes atomic-scale DFT results for the thermodynamic energy landscape characterizing metastable reaction intermediates in the conversion of adsorbed O to O_i in the deep bulk. The geometry for chemisorbed O_{ads} (Figure 2(b-1)) reproduces that reported in previous literature.[35] The adsorbed O forms two bonds to underlying surface atoms: one to surface O with a length of 1.53 Å and one to surface Zn with a length of 2.04 Å. The latter number nearly equals the average O-Zn bond length of 2.01 – 2.02 Å within the surface layer.

When residing in the first layer below the surface, the defect forms another neutral dumbbell structure (Figure 2(b-2)), with an O-O bond of length 1.48 Å. In accord with previous literature,[9] the two remaining bonds between the injecting O atom and nearby Zn atoms have lengths in the range 1.95 – 1.97 Å, which is 3% shorter than the corresponding bond length in the deep bulk. The defect diffuses further into the bulk by successive hops (Figure 2(b-3)) with bond lengths that lengthen progressively toward deep-bulk values.

Figure 3 shows an activation barrier diagram (with corresponding geometries) at key points along the reaction coordinate for interchange between O_{ads} and O_i in the first sublayer. Rightward movement along the reaction coordinate corresponds to injection; leftward corresponds to annihilation. The activation energy in the injection direction equals 1.19 eV, while that in the annihilation direction is 0.81 eV. Analogous to O_i hopping in deep-bulk ZnO,[9] the transition state exhibits a neutral dumbbell geometry. The O-O bond length is 1.59 Å. The three O atoms neighboring the defect bond to nearby Zn atoms with lengths ranging between 1.89 and 2.44 Å.

3. Mesoscale modeling

Figure 4 shows Arrhenius plots of F and D_{tr} obtained from the classical equilibrium model, and Figure 5 shows the variation of these quantities with P_{O_2}. There is only a weak dependence on T and negligible dependence on P_{O_2}. Table 1 lists the effective activation energy and pre-exponential factor for F and D_{tr}, together with the exponent b to which P_{O_2} must be raised in a pressure dependence of the form $P_{O_2}{}^{b}$.

Table 2 details the initial and optimized thermodynamic and kinetic parameters from the microkinetic model. The initial values originated from an earlier version of the model for ZnO(0001)[57] or from educated guesses. Figure 1(b) presents a representative simulated ^{18}O profile (570 ^{o}C and $P_{O_2}= 5 \times 10^{-5}$ Torr) together with its experimental counterpart. The microkinetic simulations generally reproduce the experimental profiles satisfactorily. In addition to the classical equilibrium results for F and D_{tr}, Figure 4 shows the temperature variation of these quantities obtained by combining the appropriate elementary parameters from the microkinetic model. Figure 5 displays the variation of the composite quantities with P_{O_2}. Table 1 shows the effective activation energy and pre-exponential factor computed from the microkinetic parameters for F and D_{tr}, together with the exponent b.

Discussion

1. Special features of interstitialcy mechanism

O_i in many oxides forms a symmetric dumbbell or split configuration (including or missing an O-O bond, respectively), wherein two O atoms are associated with a lattice site that would normally host only one. This structure characterizes not only ZnO but also rutile[15,73] and anatase[74] TiO_2, SnO_2,[75] MgO,[76] CeO_2,[77,78] monoclinic HfO_2,[79] and α-Al_2O_3.[80–82] Diffusional hopping occurs via an interstitialcy mechanism, wherein one of the two atoms moves to a

neighboring lattice site to form an identical configuration. The two O atoms within the defect have equal probabilities of hopping.

Under O-rich conditions, the hopping barrier itself is typically quite modest in semiconducting oxides exhibiting O_i-governed diffusion. For example, the barrier lies below 1 eV in ZnO,[8,16,26,27] TiO_2,[83,84] MgO,[85] ZrO_2,[86] HfO_2,[87] UO_2,[88,89] CeO_2,[90] Ga_2O_3,[91] $La_2NiO_{4+\delta}$,[92,93] $La_2CoO_{4+\delta}$,[93] $Y_{1-x}Zr_xMnO_{3+\delta}$,[94] $Pr_2NiO_{4+\delta}$,[95] and $La_{2-x}Sr_xNiO_{4+\delta}$.[96] Barriers below 1 eV enable significant defect diffusion rates even at room temperature. For example, a hopping barrier of 0.7 eV and a pre-exponential of 0.01 $cm^2\ s^{-1}$ leads to a random-walk diffusion length ($\sqrt{6D_{\mathrm{hop}}t}$) of nearly 900 nm at 25°C and time t = 1 day.

These low barriers, together with the hopping statistics described above, lead to important consequences for mesoscale diffusion of an isotopic label that differ considerably from those of a vacancy mechanism in ZnO and possibly many other semiconducting oxides. These manifestations appear to have been largely unrecognized up to now, and include the possibility of large differences in the effective hopping rate for ^{16}O and ^{18}O, and the need for microkinetic models to incorporate sequestration sites for O_i other than the lattice.

1.a. Effects of interstitialcy hopping statistics on movement of ^{16}O vs ^{18}O

Prior theoretical literature has shown[97] that the variance of isotopic tracer spreading by an interstitialcy mechanism exhibits dynamics like those of vacancy-mediated diffusion. It has not been recognized until recently,[23] however, that D_{hop} measured by isotopic labeling does not equal the "true" tracer diffusivity of unlabeled interstitials. The inequality stems from the high symmetry of the defect.

The high symmetry implies that either O atom within the interstitial hops with equal probability. Thus, any particular atom (^{18}O or ^{16}O) finding itself within an interstitial can execute

only 2-3 hops on average before becoming temporarily immobilized in the lattice. For example, the likelihood of a given atom surviving in a mobile state after two hops is $0.5^2 = 0.25$. Remaining mobile after three hops has a likelihood of only $0.5^3 = 0.125$.

Such statistics govern the immobilization of any particular atom regardless of whether it is labeled. However, each hopping event conserves O_i as a chemical species; only the constituent atoms change. For dilute label concentrations (0.2-1% here) most lattice O is mass 16. Thus, immobilization of ^{18}O usually mobilizes a lattice ^{16}O. However, immobilization of ^{16}O usually releases another ^{16}O. Indeed, ^{16}O atoms traverse the solid for many atomic diameters before finally liberating an ^{18}O atom and breaking the 16-dominated chain. Only rarely can immobilization of ^{18}O release another ^{18}O in a similar fashion.

If D_{hop} denotes the hopping diffusivity of O_i in a hypothetical single-isotope solid (or equivalently, computed by DFT), then the statistical effects just described imply an effective hopping diffusivity for the ^{18}O label of $[^{18}O_i]/([^{18}O_i]+[^{16}O_i])D_{hop}$. For dilute labels, the statistical factor may scale D_{hop} by several orders of magnitude depending upon the degree of dilution. No equivalent effect occurs for a vacancy mechanism because the defect includes only a single entity (the missing atom) rather than a symmetric pair of equivalent atoms.

1.b. Implications of low interstitialcy barriers for sequestration of O_i

Self-diffusion experiments render the isotopic label mobile at the diffusion temperature, but the label stops moving upon quenching. Long-term profile stability toward shelf storage at room temperature is commonplace for vacancy-mediated diffusion. We have also observed such stability in interstitialcy-mediated diffusion systems, including the present case of ZnO. However, the underlying reason for stability differs for the two kinds of mechanisms – with an important implication for isotopic profile interpretation and microkinetic modeling.

Vacancy mechanisms in semiconducting oxides typically exhibit hopping barriers above about 1 eV (with notable exceptions such as, strontium titanate[98]). With such substantial barriers, profile immobilization at room temperature can occur by simple freezing of the vacancies in place.

In contrast, O_i with hopping barriers below about 1 eV retain significant diffusion rates at room temperature as indicated above. For interstitialcy-governed diffusion, long-term stability of isotopic profiles implies that O_i must disappear as a chemical species upon quenching to room temperature and that sequestration sites for O_i must exist in concentrations sufficient to capture the interstitials. Possible sites for sequestration include numerous kinds of extended defects and small defect clusters. Extended defects such as dislocations populate many semiconducting oxides including ZnO, although their interaction kinetics with O_i have received scant attention. Small clusters of self-interstitials have been examined in some semiconducting oxides,[88,99–101] but in less detail than in elemental semiconductors such as Si.[102,103] The reported interstitial clusters in ZnO [104,105] do not involve oxygen, although complexes of O_i with zinc vacancies and extrinsic hydrogen (which is ubiquitous in many oxides including ZnO[106]) seem intuitively possible.

The result of both vacancy and interstitialcy mechanisms – stable profiles at room temperature – may seem identical, but the implications differ for profile interpretation. For an interstitialcy mechanism, the sites responsible for sequestering O_i at room temperature also slow the movement of O_i at diffusion temperatures by successive capture and release events. Microkinetic models need to account for such sites explicitly. Since vacancies require no sequestration at room temperature to yield stable profiles, microkinetic models typically do not need to incorporate separate sequestration sites.

2. Mesoscale modeling

2.1. Microkinetic model

2.1.1. Microkinetic bulk parameters

As shown in Table 2, the microkinetic simulations yield 0.44 ± 0.05 eV and 7.7 ± 0.7 k_B respectively for the formation enthalpy (ΔH_f) and entropy (ΔS_f) of O_i. The value for ΔH_f is rather low. Since ΔH_f depends upon the oxygen chemical potential $\Delta\mu_O$, comparisons of ΔH_f with DFT values requires accounting for the value of $\Delta\mu_O$ in the experiments. For neutral O_i, $\Delta\mu_O$ can vary between limits of zero (maximally O-rich) and –3.42 eV (maximally Zn-rich) per formula unit. Our experimental conditions correspond to $\Delta\mu_O$ = –1.16 eV, which lies closer to the O-rich side of the continuum. For neutral dumbbell O_i under maximally O-rich conditions, literature values of DFT formation energies vary between 1 – 1.65 eV.[8,9,11,45] Accounting for $\Delta\mu_O$ in our experiments adds 1.16 eV to these values, making them considerably larger than the value of 0.44 eV in Table 2.

Unexpectedly low estimates for ΔH_f have resulted from other microkinetic studies involving symmetric split interstitial species, including O_i in ZnO(0001),[57] O_i in TiO_2(110)[62] and the silicon interstitial in Si.[107] The profiles in Figure 1 exhibit very little T dependence, suggesting a small variation in [O_i]. The weak T dependence of [O_i] leads to small effective values for ΔH_f, and probably arises from the effects of surface processes leading up to formation of injectable O together with the interaction between O_i and sequestration sites.

By contrast, the microkinetic hopping barrier (E_{hop}) of 0.89 $\pm$ 0.08 eV agrees closely with DFT values for O_i^0 of 0.9–1.0 eV.[9,12,65] The microkinetic hopping prefactor ($D_{0,hop}$) of (3.25±0.32)×10^{-3} cm^2 s^{-1} lies in a typical range for this quantity.

The formation enthalpy (ΔH_{fs}) and prefactor (S_{tot}) for the sequestration sites respectively equal 1.2±0.12 eV and (2.13±0.2) × 10^{30} atoms cm^{-3}, with a pressure exponent c = 0.45 These numbers lead to a concentration [S] of 4.1×10^{20} cm^{-3} at 600 °C and 5×10^{-5} Torr. As indicated above, we surmise these sites could include H in all its forms (interstitial, substitutional, and H_2 molecules),[108–110] zinc vacancies V_{Zn}, and/or extended defects

The sequestration complexes liberate O_i with an activation energy (E_{diss}) of 1.6 ± 0.1 eV. For TiO_2, the extended defects liberate O_i with an activation energy of 3.3 eV, which is higher by almost a factor of two.[84] The comparison is imperfect because of the difference in the identity of the solids, but the disparity may also originate from the sizes of the defect clusters. Generally speaking, such barriers depend upon the size of the defect complexes.[66,103,111–113] For example, the dissociation energy for Si interstitials from clusters in silicon varies from 3.1 eV to 4.0 eV as the complexes become larger.[103,112] The complexes hypothesized here are small, which would presumably lead to dissociation barriers near the bottom of that range – in line with the actual observation. For the pre-exponential factor, the microkinetic model and previous literature both point to values lying near the Debye frequency.[66,84]

2.1.2. Microkinetic surface parameters

The DFT results of Figure 2 show that injection into the 1st atomic layer below the surface occurs with an activation barrier of 1.19 eV. The confidence with which DFT rate constants may be compared to those from microkinetic modeling has been detailed elsewhere[15,23] but typical random uncertainties for both approaches lie near 0.1 eV. Given these uncertainties, the DFT value matches the microkinetic estimate for E_{inj} of 1.0±0.1 eV. Additional computations for hopping of O_i^0 into the 2nd and 3rd layers yield slightly lower barriers of 1.0 eV, which

indicates that the first hop into the bulk limits the rate. The pre-exponential factor ν_{inj} for ZnO($10\bar{1}0$) converges to a value near a conventional Debye frequency of (1.0±0.5)×10^{13} s^{-1}.

Under the O-rich conditions of the experiments, oxygen adsorbs on nonpolar ZnO($10\bar{1}0$) via a neutral dumbbell configuration with a maximum coverage of 0.5 ML[35] referenced to the concentration of all oxygen-containing sites in the surface layer. The numerical value of the maximum surface concentration n_{sat} of adsorbed O atoms is therefore 1.68×10^{14} cm^{-2}. As indicated by Figure S4(b) in the ESI, the computed coverage of injectable oxygen is low, with θ << 0.1. In this limit, n_{sat} and the zero-coverage annihilation probability S_0 cannot be deconvolved by microkinetic modeling.[62] However, the value of 7.5×10^{7} cm^{-2} for the mathematical product $n_{\mathrm{sat}} \times S_0$ leads to S_0 = 4.5 × 10^{-7} based upon n_{sat} = 1.68×10^{14} cm^{-2}. This low value for S_0 accords with the high stability of pristine ZnO($10\bar{1}0$), which resists the addition of oxygen atoms from either the gas phase above or the bulk solid below.

The DFT barrier for hopping from the 1st subsurface layer into the surface layer is only 0.81 eV, which falls below the value of 0.9–1.0 eV for bulk hopping. The rate-limiting activation energy for O_i annihilation at the surface therefore equals that for bulk hopping.

2.2. Comparison to classical equilibrium model

Table 1 shows the effective activation energies, prefactors, and the exponent b in $P_{O_2}^{b}$ for the parameters F and D_{tr} computed directly from the classical equilibrium model and indirectly from the microkinetic parameters in Table 2. As discussed elsewhere,[62] the microkinetic confidence intervals are tighter than the analytical ones because of differences in the method of data aggregation. The effective parameters for D_{tr} from the classical thermodynamic and microkinetic approaches match very closely. For F, however, the microkinetic values exhibit noticeably stronger dependences upon T and P_{O_2}. Figure 4 represents these similarities and

differences in graphical form. For D_{tr}, the lines from the analytical and microkinetic approaches overlay almost perfectly. For F, the general magnitudes of the two lines compare rather well, although the microkinetic versions exhibit larger slopes.

The exponent b describing the pressure dependence of D_{tr} is very small (0.03–0.05) for the both the classical and microkinetic approaches. The dependence of D_{tr} upon P_{O_2} depends largely upon the quotient $[O_i]/[S_C]$. With the assumptions of thermodynamic equilibrium and a neutral charge state for O_i, $[O_i]$ varies according to the formation stoichiometry $O_2(gas) \rightarrow 2O_i$, which leads to a pressure exponent 0.5. Table 2 shows that the pressure exponent for forming S is c = 0.45. The aggregate pressure dependence of $[O_i]/[S_C]$ therefore represents the mathematical difference between the exponent of 0.5 for O_i and c = 0.45 for S_C, leading to a microkinetic prediction of b = 0.05.

Similarly, the activation energy for D_{tr} simplifies at low coverage ($\theta << 1$) to $E_{diff} + \Delta H_f - \Delta H_{fs}$ based on Eq. (S11) in the ESI. The microkinetic result (0.13 eV) exactly matches the analytical activation energy of 0.13 eV.

For F, the classical and microkinetic approaches exhibit poorer agreement. The profiles themselves show very little dependence upon either P_{O_2} or T. The classical thermodynamic value of b = 0.02 lies far below the corresponding microkinetic value of 0.5. Similarly, the classical activation energy of 0.23 eV lies well below the microkinetic value of 1.32 eV.

A closer examination shows why F varies so strongly in the microkinetic framework. In the limit of low θ, $r_{inj} >> r_{ann}$ and combination of Eqs. (S15)–(S17) in the ESI shows that F for the isotope simplifies to

$$F_{18} \approx \nu_{inj} e^{-E_{inj}/k_B T} n_{sat} \theta = \nu_{inj} e^{-E_{inj}/k_B T} n_{sat} \frac{3 D_{hop} S_0 [O_i]_{x=0}}{l \nu_{inj} e^{-E_{inj}/k_B T} n_{sat}} = \frac{3 D_{hop} S_0 [^{18}O_i]}{l} \qquad (9).$$

This expression contains no quantities connecting to the sequestration mechanism. The only variation with P_{O_2} and T occurs through bulk quantities including [$^{18}O_i$] and D_{hop}. Surface-related quantities such as S_0 and n_{sat} remain constant. As indicated above, formation stoichiometry leads inevitably to a pressure exponent 0.5 in [$^{18}O_i$] and therefore F. In an analogous way, the activation energy for F is constrained by Eqs. (S15) and (S16) to vary as $E_{hop} + \Delta H_f = 1.32$ eV. In short, thermodynamic equilibrium and conventional rate expressions for the rates of hopping, injection and annihilation, impose severe constraints on the microkinetic model's ability to reproduce the P_{O_2} and T dependence of the profiles.

3. Comparison to other surfaces

Direct comparison of the injection barrier with microkinetic values from the existing literature for polar Zn-term (0001) suffers from considerable systematic uncertainty. The microkinetic value[57] of $E_{inj} = 2.0 \pm 0.2$ eV for Zn-ZnO(0001) employed a different model, and the DFT value[16] of 1.67±0.32 eV pertained to O_i^0 but placed the final state in an octahedral site rather than a dumbbell.

Yet certain aspects of the results for nonpolar ZnO($10\bar{1}0$) may be compared with polar Zn-term ZnO(0001) and O-term ZnO($000\bar{1}$). The nonpolar and O-term surfaces share minimal T dependence in their profiles. Indeed, the O-term surface yields no T dependence at all in any parameter, whereas the nonpolar surface shows a weak but nonzero dependence in F. The magnitudes of D_{tr} for the two surfaces lie close to each other as well. By contrast, the Zn-term surface exhibits strongly T-dependent behavior, with an activation for F in the range 1.3–1.7 eV.[16,17,57] The general magnitude of D_{tr} lies in the same general range as for the nonpolar surface, however. As indicated in the ESI, anisotropy exists between hopping in the c and a directions. However, this anisotropy does not explain the differences in F because O-term and Zn-term

surfaces both involve *c*-axis diffusion. The principal differences in behavior originate from intrinsic differences in the injection barrier and/or adsorption processes that create injectable O.

Comparison of the present results for nonpolar ZnO to those for nonpolar TiO_2 published elsewhere[23] yields additional insights. Despite considerably different injection mechanisms, both surfaces exhibit injection barriers only 0.1–0.2 eV higher than for bulk site hopping. Annihilation barriers in both cases equal those for site hopping. The hopping barriers for both solids lie below 1 eV, and in principle enable nanometer-scale diffusion lengths only a few tens of degrees above room temperature. For example, given the diffusion parameters listed in Table 2, the random-walk diffusion length for O_i corresponding to $\sqrt{6D_{\mathrm{hop}}t}$ at 50°C for 1 hour equals 10 nm. Those rates of diffusion could enable defect engineering under very modest conditions.

Conclusions

Despite differing O_i injection mechanisms for nonpolar ZnO and TiO_2 surfaces, both cases exhibit injection barriers only 0.1–0.2 eV higher than for bulk site hopping. Bulk hopping barriers for O_i slightly lie below 1 eV in many oxides, and therefore enable nanometer-scale diffusion lengths only a few tens of degrees above room temperature. In addition, low hopping barriers coupled with statistical considerations lead to important qualitative manifestations in diffusion via an interstitialcy mechanism that do not occur for vacancies. Evidence is building that, as long as the surface remains free from of poisoning foreign adsorbates, facile defect injection and annihilation may occur readily at such modest temperatures for a broad variety of semiconducting oxides. If future work bears out this possibility for other materials and for polar surfaces, the prospects become much brighter for post-synthesis control of V_O in a variety of applications.

Conflicts of interest

There are no conflicts to declare.

Acknowledgements

This work was supported by the U.S. National Science Foundation under grant DMR 17-09327. Computational resources were provided by the Illinois Campus Cluster Program (ICCP) in conjunction with the National Center for Supercomputing Applications (NCSA) and which is supported by funds from the University of Illinois at Urbana-Champaign. SIMS was performed in the Materials Research Laboratory Central Research Facilities, University of Illinois at Urbana-Champaign.

References

1 M. Zhang, F. Averseng, J.-M. Krafft, P. Borghetti, G. Costentin and S. Stankic, Controlled Formation of Native Defects in Ultrapure ZnO for the Assignment of Green Emissions to Oxygen Vacancies, *J. Phys. Chem. C*, 2020, **124**, 12696–12704.

2 S. G. Kumar and K. S. R. K. Rao, Zinc oxide based photocatalysis: tailoring surface-bulk structure and related interfacial charge carrier dynamics for better environmental applications, *Rsc Adv.*, 2015, **5**, 3306–3351.

3 X. Li, J. Song, Y. Liu and H. Zeng, Controlling oxygen vacancies and properties of ZnO, *Curr. Appl. Phys.*, 2014, **14**, 521–527.

4 D. Zhu, Q. Cao, R. Qiao, S. Zhu, W. Yang, W. Xia, Y. Tian, G. Liu and S. Yan, Oxygen vacancies controlled multiple magnetic phases in epitaxial single crystal Co 0.5 (Mg 0.55 Zn 0.45) 0.5 O 1-v thin films, *Sci. Rep.*, 2016, **6**, 24188.

5 K. C. Verma, N. Goyal and R. K. Kotnala, Lattice defect-formulated ferromagnetism and UV photo-response in pure and Nd, Sm substituted ZnO thin films, *Phys. Chem. Chem. Phys.*, 2019, **21**, 12540–12554.

6 D. Kim, K. Y. Lee, M. K. Gupta, S. Majumder and S. Kim, Self-compensated insulating ZnO-based piezoelectric nanogenerators, *Adv. Funct. Mater.*, 2014, **24**, 6949–6955.

7 Y. Tu, S. Chen, X. Li, J. Gorbaciova, W. P. Gillin, S. Krause and J. Briscoe, Control of oxygen vacancies in ZnO nanorods by annealing and their influence on ZnO/PEDOT: PSS diode behaviour, *J. Mater. Chem. C*, 2018, **6**, 1815–1821.

8 P. Erhart, K. Albe and A. Klein, First-principles study of intrinsic point defects in ZnO: Role of band structure, volume relaxation, and finite-size effects, *Phys. Rev. B*, 2006, **73**, 205203.

9 A. Janotti and C. G. Van de Walle, Native point defects in ZnO, *Phys. Rev. B*, 2007, **76**, 165202.

10 R. Vidya, P. Ravindran, H. Fjellvåg, B. G. Svensson, E. Monakhov, M. Ganchenkova and R. M. Nieminen, Energetics of intrinsic defects and their complexes in ZnO investigated by density functional calculations, *Phys. Rev. B*, 2011, **83**, 45206.

11 A. Goyal, P. Gorai, H. Peng, S. Lany and V. Stevanović, A computational framework for automation of point defect calculations, *Comput. Mater. Sci.*, 2017, **130**, 1–9.

12 G. Y. Huang, C. Y. Wang and J. T. Wang, First-principles study of diffusion of oxygen vacancies and interstitials in ZnO, *J. Phys. Condens. Matter*, 2009, **21**, 195403.

13 A. Janotti and C. G. Van de Walle, Fundamentals of zinc oxide as a semiconductor, *Reports Prog. Phys.*, 2009, **72**, 126501.

14 D. Chen, F. Gao, M. Dong and B. Liu, Migration of point defects and a defect pair in zinc oxide using the dimer method, *J. Mater. Res.*, 2012, **27**, 2241–2248.

15 H. Jeong, E. G. Seebauer and E. Ertekin, First-principles description of oxygen self-diffusion in rutile TiO2: Assessment of uncertainties due to enthalpy and entropy contributions, *Phys. Chem. Chem. Phys.*, 2018, **20**, 17448–17457.

16 P. Gorai, E. Ertekin and E. G. Seebauer, Surface-assisted defect engineering of point defects in ZnO, *Appl. Phys. Lett.*, 2016, **108**, 241603.

17 M. Li and E. G. Seebauer, Surface-Based Control of Oxygen Interstitial Injection into ZnO via Submonolayer Sulfur Adsorption, *J. Phys. Chem. C*, 2016, **120**, 23675–23682.

18 G. Kresse, O. Dulub and U. Diebold, Competing stabilization mechanism for the polar ZnO (0001)-Zn surface, *Phys. Rev. B*, 2003, **68**, 245409.

19 O. Dulub, U. Diebold and G. Kresse, Novel stabilization mechanism on polar surfaces: ZnO (0001)-Zn, *Phys. Rev. Lett.*, 2003, **90**, 16102.

20 M. Valtiner, M. Todorova, G. Grundmeier and J. Neugebauer, Temperature stabilized surface reconstructions at polar ZnO (0001), *Phys. Rev. Lett.*, 2009, **103**, 65502.

21 M. Valtiner, M. Todorova and J. Neugebauer, Hydrogen adsorption on polar ZnO(0001)-Zn: Extending equilibrium surface phase diagrams to kinetically stabilized structures, *Phys. Rev. B - Condens. Matter Mater. Phys.*, 2010, **82**, 1–6.

22 J. V Lauritsen, S. Porsgaard, M. K. Rasmussen, M. C. R. Jensen, R. Bechstein, K. Meinander, B. S. Clausen, S. Helveg, R. Wahl and G. Kresse, Stabilization principles for polar surfaces of ZnO, *ACS Nano*, 2011, **5**, 5987–5994.

23 H. Jeong, E. Ertekin and E. G. Seebauer, Kinetic Control of Oxygen Interstitial Interaction with TiO2(110) via the Surface Fermi Energy, *Langmuir*, 2020, **36**, 12632–12648.

24 F. Bénière, Tracer diffusion techniques, *J. Chem. Soc. Faraday Trans.*, 1990, **86**, 1151–1156.

25 R. A. De Souza and M. Martin, Probing diffusion kinetics with secondary ion mass spectrometry, *MRS Bull.*, 2009, **34**, 907–914.

26 J. A. Kilner, S. J. Skinner and H. H. Brongersma, The isotope exchange depth profiling (IEDP) technique using SIMS and LEIS, *J. Solid State Electrochem.*, 2011, **15**, 861–876.

27 P. Hohenberg and W. Kohn, Inhomogeneous electron gas, *Phys. Rev.*, 1964, **136**, B864.

28 W. Kohn and L. J. Sham, Self-consistent equations including exchange and correlation effects, *Phys. Rev.*, 1965, **140**, A1133.

29 G. Kresse and J. Furthmüller, Efficiency of ab-initio total energy calculations for metals and semiconductors using a plane-wave basis set, *Comput. Mater. Sci.*, 1996, **6**, 15–50.

30 G. Kresse and J. Furthmüller, Efficient iterative schemes for ab initio total-energy calculations using a plane-wave basis set, *Phys. Rev. B*, 1996, **54**, 11169–11186.

31 G. Kresse and D. Joubert, From ultrasoft pseudopotentials to the projector augmented-wave method, *Phys. Rev. B*, 1999, **59**, 1758–1775.

32 J. P. Perdew, K. Burke and M. Ernzerhof, Generalized Gradient Approximation Made Simple, *Phys. Rev. Lett.*, 1996, **77**, 3865–3868.

33 Y. Yan and M. M. Al-Jassim, Structure and energetics of water adsorbed on the ZnO(10$\bar{1}$0) surface, *Phys. Rev. B - Condens. Matter Mater. Phys.*, 2005, **72**, 1–6.

34 B. Meyer, H. Rabaa and D. Marx, Water adsorption on ZnO(10$\bar{1}$0): From single molecules to partially dissociated monolayers, *Phys. Chem. Chem. Phys.*, 2006, **8**, 1513–1520.

35 P. Gorai, E. G. Seebauer and E. Ertekin, Mechanism and energetics of O and O2 adsorption on polar and non-polar ZnO surfaces, *J. Chem. Phys.*, 2016, **144**, 184708.

36 Y. Yan, M. M. Al-Jassim and S.-H. Wei, Oxygen-vacancy mediated adsorption and reactions of molecular oxygen on the $\mathrm{ZnO}(10\overline{1}0)$ surface, *Phys. Rev. B*, 2005, **72**, 161307.

37 A. G. Saputro, F. T. Akbar, N. P. P. Setyagar, M. K. Agusta, A. D. Pramudya and H. K. Dipojono, Effect of surface defects on the interaction of the oxygen molecule with the ZnO(10$\bar{1}$0) surface, *New J. Chem.*, 2020, **44**, 7376–7385.

38 C. Wöll, The chemistry and physics of zinc oxide surfaces, *Prog. Surf. Sci.*, 2007, **82**, 55–120.

39 H. F. Wen, M. Miyazaki, Q. Zhang, Y. Adachi, Y. J. Li and Y. Sugawara, Direct observation of atomic step edges on the rutile TiO 2 (110)-(1× 1) surface using atomic

force microscopy, *Phys. Chem. Chem. Phys.*, 2018, **20**, 28331–28337.
40 W. H. Cheng and H. H. Kung, Interaction of CO, CO2 and O2 with nonpolar, stepped and polar Zn surfaces of ZnO, *Surf. Sci.*, 1982, **122**, 21–39.
41 G. Henkelman, B. P. Uberuaga and H. Jónsson, A climbing image nudged elastic band method for finding saddle points and minimum energy paths, *J. Chem. Phys.*, 2000, **113**, 9901–9904.
42 F. Oba, M. Choi, A. Togo, A. Seko and I. Tanaka, Native defects in oxide semiconductors: a density functional approach, *J. Phys. Condens. Matter*, 2010, **22**, 384211.
43 H. Jeong, E. G. Seebauer and E. Ertekin, Fermi Level Dependence of Gas-Solid Oxygen Defect Exchange Mechanism on TiO2 (110) by First-Principles Calculations, *J. Chem. Phys.*, 2020, **153**, 124710.
44 J. L. Lyons, J. B. Varley, D. Steiauf, A. Janotti and C. G. Van De Walle, First-principles characterization of native-defect-related optical transitions in ZnO, *J. Appl. Phys.*, 2017, **122**, 035704.
45 A. A. Sokol, S. A. French, S. T. Bromley, C. R. A. Catlow, H. J. J. van Dam and P. Sherwood, Point defects in ZnO, *Faraday Discuss.*, 2007, **134**, 267–282.
46 D. Shaw, in *Springer Handbook of Electronic and Photonic Materials*, Springer, 2017, p. 1.
47 J. Maier, Mass transport in the presence of internal defect reactions—concept of conservative ensembles: I, chemical diffusion in pure compounds, *J. Am. Ceram. Soc.*, 1993, **76**, 1212–1217.
48 J. Maier, Mass transport in the presence of internal defect reactions—Concept of conservative ensembles: IV, Tracer diffusion and intercorrelation with chemical diffusion and ion conductivity, *J. Am. Ceram. Soc.*, 1993, **76**, 1228–1232.
49 J. Maier, On the correlation of macroscopic and microscopic rate constants in solid state chemistry, *Solid State Ionics*, 1998, **112**, 197–228.
50 J. Maier, Interaction of oxygen with oxides:: How to interpret measured effective rate constants?, *Solid State Ionics*, 2000, **135**, 575–588.
51 J. Claus, M. Leonhardt and J. Maier, Tracer diffusion and chemical diffusion of oxygen in acceptor doped SrTiO3, *J. Phys. Chem. Solids*, 2000, **61**, 1199–1207.
52 P. S. Manning, J. D. Sirman and J. A. Kilner, Oxygen self-diffusion and surface exchange studies of oxide electrolytes having the fluorite structure, *Solid State Ionics*, 1996, **93**, 125–132.
53 J. Blair and D. S. Mebane, A Bayesian approach to electrical conductivity relaxation and isotope exchange/secondary ion mass spectrometry, *Solid State Ionics*, 2015, **270**, 47–53.
54 M. V Ananyev, E. S. Tropin, V. A. Eremin, A. S. Farlenkov, A. S. Smirnov, A. A. Kolchugin, N. M. Porotnikova, A. V Khodimchuk, A. V Berenov and E. K. Kurumchin, Oxygen isotope exchange in La 2 NiO 4±δ, *Phys. Chem. Chem. Phys.*, 2016, **18**, 9102–9111.
55 J. A. Kilner, R. A. De Souza and I. C. Fullarton, Surface exchange of oxygen in mixed conducting perovskite oxides, *Solid State Ionics*, 1996, **86**, 703–709.
56 P. Fielitz and G. Borchardt, Oxygen exchange at gas/oxide interfaces: how the apparent activation energy of the surface exchange coefficient depends on the kinetic regime, *Phys. Chem. Chem. Phys.*, 2016, **18**, 22031–22038.
57 M. Li and E. G. Seebauer, Microkinetic Model for Oxygen Interstitial Injection from the ZnO (0001) Surface into the Bulk, *J. Phys. Chem. C*, 2018, **122**, 2127–2136.

58 V. Moroz, Y.-S. Oh, D. Pramanik, H. Graoui and M. A. Foad, Optimizing boron junctions through point defect and stress engineering using carbon and germanium co-implants, *Appl. Phys. Lett.*, 2005, **87**, 51908.

59 A. Sibaja-Hernandez, M. W. Xu, S. Decoutere and H. Maes, TSUPREM-4 based modeling of boron and carbon diffusion in SiGeC base layers under rapid thermal annealing conditions, *Mater. Sci. Semicond. Process.*, 2005, **8**, 115–120.

60 S. K. Theiss, M.-J. Caturla, T. D. de la Rubia, M. C. Johnson, A. Uralt and P. B. Griffin, Linking ab initio energetics to experiment: Kinetic Monte Carlo simulation of transient enhanced diffusion of B in Si, *MRS Online Proc. Libr. Arch.*, , DOI:https://doi.org/10.1557/PROC-538-291.

61 J. Kim and T. Won, Atomistic modelling for boron diffusion profile in silicon posterior to germanium pre-amorphization, *Microelectron. Eng.*, 2007, **84**, 1556–1561.

62 K. M. Pangan-Okimoto, P. Gorai, A. G. Hollister and E. G. Seebauer, Model for oxygen interstitial injection from the rutile TiO2 (110) surface into the bulk, *J. Phys. Chem. C*, 2015, **119**, 9955–9965.

63 K. L. Gilliard-AbdulAziz and E. G. Seebauer, Microkinetic Model for Reaction and Diffusion of Titanium Interstitial Atoms near a TiO2 (110) Surface, *Phys. Chem. Chem. Phys.*, 2018, **20**, 4587–4596.

64 P. Gorai, A. G. Hollister and E. G. Seebauer, Measurement of defect-mediated oxygen self-diffusion in metal oxides, *ECS J. Solid State Sci. Technol.*, 2012, **1**, Q21–Q24.

65 P. Erhart and K. Albe, First-principles study of migration mechanisms and diffusion of oxygen in zinc oxide, *Phys. Rev. B*, 2006, **73**, 115207.

66 R. Gunawan, M. Y. L. Jung, R. D. Braatz and E. G. Seebauer, Parameter Sensitivity Analysis Applied to Modeling Transient Enhanced Diffusion and Activation of Boron in Silicon, *J. Electrochem. Soc.*, 2003, **150**, G758.

67 R. J. Chater, S. Carter, J. A. Kilner and B. C. H. Steele, Development of a novel SIMS technique for oxygen self-diffusion and surface exchange coefficient measurements in oxides of high diffusivity, *Solid State Ionics*, 1992, **53**, 859–867.

68 J. Rutman, M. Kilo, S. Weber and I. Riess, Tracer surface exchange and diffusion of oxygen in nano crystals of Gd doped CeO2, *Solid State Ionics*, 2014, **265**, 29–37.

69 P. Gorai and E. G. Seebauer, Electric field-driven point defect pile-up near ZnO polar surfaces, *Solid State Ionics*, 2017, **301**, 95–98.

70 P. Gorai and E. G. Seebauer, Kinetic model for electric-field induced point defect redistribution near semiconductor surfaces, *Appl. Phys. Lett.*, 2014, **105**, 21604.

71 P. Gorai, Y. V Kondratenko and E. G. Seebauer, Mechanism and kinetics of near-surface dopant pile-up during post-implant annealing, *J. Appl. Phys.*, 2012, **111**, 94510.

72 P. Gorai, A. G. Hollister and E. G. Seebauer, Electrostatic drift effects on near-surface defect distribution in TiO2, *Appl. Phys. Lett.*, 2013, **103**, 141601.

73 H.-Y. Lee, S. J. Clark and J. Robertson, Calculation of point defects in rutile TiO2 by the screened-exchange hybrid functional, *Phys. Rev. B*, 2012, **86**, 75209.

74 S. Na-Phattalung, M. F. Smith, K. Kim, M.-H. Du, S.-H. Wei, S. B. Zhang and S. Limpijumnong, First-principles study of native defects in anatase $\mathrm{Ti}{\mathrm{O}}_{2}$, *Phys. Rev. B*, 2006, **73**, 125205.

75 K. G. Godinho, A. Walsh and G. W. Watson, Energetic and Electronic Structure Analysis of Intrinsic Defects in SnO2, *J. Phys. Chem. C*, 2009, **113**, 439–448.

76 T. Brudevoll, E. A. Kotomin and N. E. Christensen, Interstitial-oxygen-atom diffusion in

MgO, *Phys. Rev. B*, 1996, **53**, 7731.
77 P. R. L. Keating, D. O. Scanlon, B. J. Morgan, N. M. Galea and G. W. Watson, Analysis of Intrinsic Defects in CeO2 Using a Koopmans-Like GGA+U Approach, *J. Phys. Chem. C*, 2012, **116**, 2443–2452.
78 T. Zacherle, A. Schriever, R. A. De Souza and M. Martin, Ab initio analysis of the defect structure of ceria, *Phys. Rev. B*, 2013, **87**, 134104.
79 A. S. Foster, F. Lopez Gejo, A. L. Shluger and R. M. Nieminen, Vacancy and interstitial defects in hafnia, *Phys. Rev. B*, 2002, **65**, 174117.
80 A. A. Sokol, A. Walsh and C. R. A. Catlow, Oxygen interstitial structures in close-packed metal oxides, *Chem. Phys. Lett.*, 2010, **492**, 44–48.
81 A. Platonenko, D. Gryaznov, Y. F. Zhukovskii and E. A. Kotomin, Ab initio simulations on charged interstitial oxygen migration in corundum, *Nucl. Instruments Methods Phys. Res. Sect. B Beam Interact. with Mater. Atoms*, 2018, **435**, 74–78.
82 Y. F. Zhukovskii, A. Platonenko, S. Piskunov and E. A. Kotomin, Ab initio simulations on migration paths of interstitial oxygen in corundum, *Nucl. Instruments Methods Phys. Res. Sect. B Beam Interact. with Mater. Atoms*, 2016, **374**, 29–34.
83 L. Tsetseris, Configurations, electronic properties, and diffusion of carbon and nitrogen dopants in rutile TiO 2: A density functional theory study, *Phys. Rev. B*, 2011, **84**, 165201.
84 K. L. Gilliard-AbdulAziz and E. G. Seebauer, Elucidating the reaction and diffusion network of oxygen interstitial atoms near a TiO2 (1 1 0) surface, *Appl. Surf. Sci.*, 2019, **470**, 854–860.
85 A.-M. El-Sayed, M. B. Watkins, T. Grasser and A. L. Shluger, Effect of electric field on migration of defects in oxides: Vacancies and interstitials in bulk MgO, *Phys. Rev. B*, 2018, **98**, 64102.
86 J. Yang, M. Youssef and B. Yildiz, Oxygen self-diffusion mechanisms in monoclinic Zr O 2 revealed and quantified by density functional theory, random walk analysis, and kinetic Monte Carlo calculations, *Phys. Rev. B*, 2018, **97**, 24114.
87 A. S. Foster, A. L. Shluger and R. M. Nieminen, Mechanism of interstitial oxygen diffusion in hafnia, *Phys. Rev. Lett.*, 2002, **89**, 225901.
88 X.-M. Bai, A. El-Azab, J. Yu and T. R. Allen, Migration mechanisms of oxygen interstitial clusters in UO2, *J. Phys. Condens. Matter*, 2012, **25**, 15003.
89 J. Yu, X.-M. Bai, A. El-Azab and T. R. Allen, Oxygen transport in off-stoichiometric uranium dioxide mediated by defect clustering dynamics, *J. Chem. Phys.*, 2015, **142**, 94705.
90 H. Y. Xiao, Y. Zhang and W. J. Weber, Stability and migration of charged oxygen interstitials in ThO2 and CeO2, *Acta Mater.*, 2013, **61**, 7639–7645.
91 M. E. Ingebrigtsen, A. Y. Kuznetsov, B. G. Svensson, G. Alfieri, A. Mihaila, U. Badstübner, A. Perron, L. Vines and J. B. Varley, Impact of proton irradiation on conductivity and deep level defects in β-Ga2O3, *APL Mater.*, 2019, **7**, 22510.
92 A. Chroneos, D. Parfitt, J. A. Kilner and R. W. Grimes, Anisotropic oxygen diffusion in tetragonal La 2 NiO 4+ δ: molecular dynamics calculations, *J. Mater. Chem.*, 2010, **20**, 266–270.
93 A. Kushima, D. Parfitt, A. Chroneos, B. Yildiz, J. A. Kilner and R. W. Grimes, Interstitialcy diffusion of oxygen in tetragonal La 2 CoO 4+ δ, *Phys. Chem. Chem. Phys.*, 2011, **13**, 2242–2249.
94 Z. L. M. Botello, A. Montenegro, N. G. Osorio, M. Huvé, C. Pirovano, D. R. Småbråten,

S. M. Selbach, A. Caneiro, P. Roussel and G. H. Gauthier, Pure and Zr-doped YMnO 3+ δ as a YSZ-compatible SOFC cathode: a combined computational and experimental approach, *J. Mater. Chem. A*, 2019, **7**, 18589–18602.

95 Z. Du, Z. Zhang, A. Niemczyk, A. Olszewska, N. Chen, K. Świerczek and H. Zhao, Unveiling the effects of A-site substitutions on the oxygen ion migration in A 2− x A′ x NiO 4+ δ by first principles calculations, *Phys. Chem. Chem. Phys.*, 2018, **20**, 21685–21692.

96 S. Xu, R. Jacobs and D. Morgan, Factors Controlling Oxygen Interstitial Diffusion in the Ruddlesden–Popper Oxide La2–x Sr x NiO4+ δ, *Chem. Mater.*, 2018, **30**, 7166–7177.

97 R. Okamoto, Y. Uno and Y. Fujitani, Self-diffusion in a lattice via the interstitialcy mechanism, *J. Phys. Soc. Japan*, 2007, **76**, 24603.

98 R. A. De Souza, Oxygen diffusion in SrTiO3 and related perovskite oxides, *Adv. Funct. Mater.*, 2015, **25**, 6326–6342.

99 B. P. Uberuaga and X.-M. Bai, Defects in rutile and anatase polymorphs of TiO2: kinetics and thermodynamics near grain boundaries, *J. Phys. Condens. Matter*, 2011, **23**, 435004.

100 X.-M. Bai and B. P. Uberuaga, Multi-timescale investigation of radiation damage near TiO2 rutile grain boundaries, *Philos. Mag.*, 2012, **92**, 1469–1498.

101 A. Soulié, G. Baldinozzi, F. Garrido and J.-P. Crocombette, Clusters of Oxygen Interstitials in UO2+ x and α-U4O9: Structure and Arrangements, *Inorg. Chem.*, 2019, **58**, 12678–12688.

102 J. W. Corbett, J. P. Karins and T. Y. Tan, Ion-induced defects in semiconductors, *Nucl. Instruments Methods*, 1981, **182**, 457–476.

103 N. E. B. Cowern, G. Mannino, P. A. Stolk, F. Roozeboom, H. G. A. Huizing, J. G. M. Van Berkum, F. Cristiano, A. Claverie and M. Jaraiz, Energetics of self-interstitial clusters in Si, *Phys. Rev. Lett.*, 1999, **82**, 4460.

104 K. Ellmer and A. Bikowski, Intrinsic and extrinsic doping of ZnO and ZnO alloys, *J. Phys. D. Appl. Phys.*, 2016, **49**, 413002.

105 M. D. McCluskey, *Defects in ZnO*, Elsevier Ltd, 2018.

106 M. D. McCluskey, M. C. Tarun and S. T. Teklemichael, Hydrogen in oxide semiconductors, *J. Mater. Res.*, 2012, **27**, 2190–2198.

107 R. Vaidyanathan, M. Y. L. Jung and E. G. Seebauer, Mechanism and energetics of self-interstitial formation and diffusion in silicon, *Phys. Rev. B - Condens. Matter Mater. Phys.*, 2007, **75**, 1–5.

108 E. V Lavrov, J. Weber, F. Börrnert, C. G. Van de Walle and R. Helbig, Hydrogen-related defects in ZnO studied by infrared absorption spectroscopy, *Phys. Rev. B*, 2002, **66**, 165205.

109 A. Janotti and C. G. Van de Walle, Hydrogen multicentre bonds, *Nat. Mater.*, 2007, **6**, 44–47.

110 J. Koßmann and C. Hättig, Investigation of interstitial hydrogen and related defects in ZnO, *Phys. Chem. Chem. Phys.*, 2012, **14**, 16392–16399.

111 L. Pelaz, M. Jaraiz, G. H. Gilmer, H.-J. Gossmann, C. S. Rafferty, D. J. Eaglesham and J. M. Poate, B diffusion and clustering in ion implanted Si: The role of B cluster precursors, *Appl. Phys. Lett.*, 1997, **70**, 2285–2287.

112 N. E. B. Cowern, G. Mannino, P. A. Stolk, F. Roozeboom, H. G. A. Huizing, J. G. M. van Berkum, F. Cristiano, A. Claverie and M. Jaraíz, Cluster ripening and transient enhanced diffusion in silicon, *Mater. Sci. Semicond. Process.*, 1999, **2**, 369–376.

113 J. Schermer, A. Martinez-Limia, P. Pichler, C. Zechner, W. Lerch and S. Paul, On a computationally efficient approach to boron-interstitial clustering, *Solid. State. Electron.*, 2008, **52**, 1424–1429.

Figures

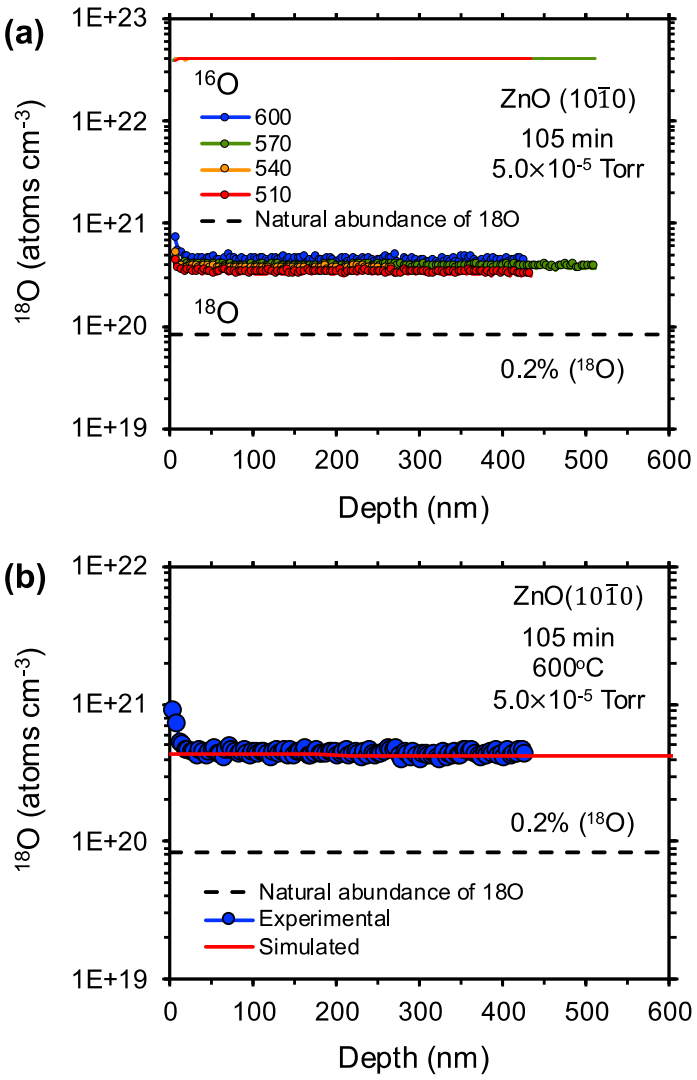

Figure 1. (a) ^{18}O diffusion profiles (symbols) and ^{16}O diffusion profiles (lines) for nonpolar ZnO(10$\bar{1}$0) with (b) a representative microkinetic model fitting (solid red line). Dashed line represents the natural abundance ^{18}O concentration (0.2%) in ZnO.

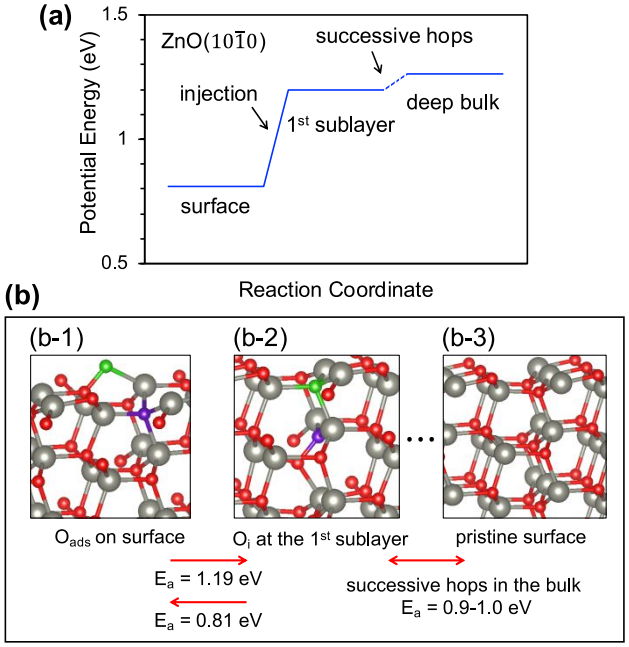

Figure 2. (a) Potential energy landscape characterizing key metastable species. Rightward movement along the reaction coordinate corresponds to the injection process; leftward corresponds to annihilation. (b) Summary of the geometries of key metastable species mediating the exchange between O adsorbed on ZnO(10$\bar{1}$0) and O_i in the deep bulk. All states are electrically neutral, and include (b-1) O_{ads}, (b-2) O in the 1st subsurface layer, and (b-3) O_i in the deep bulk. Red and gray spheres respectively designate oxygen and zinc lattice atoms. Green and purple spheres designate key participating O atoms. Site-hopping barriers originate from refs.[9,12,65].

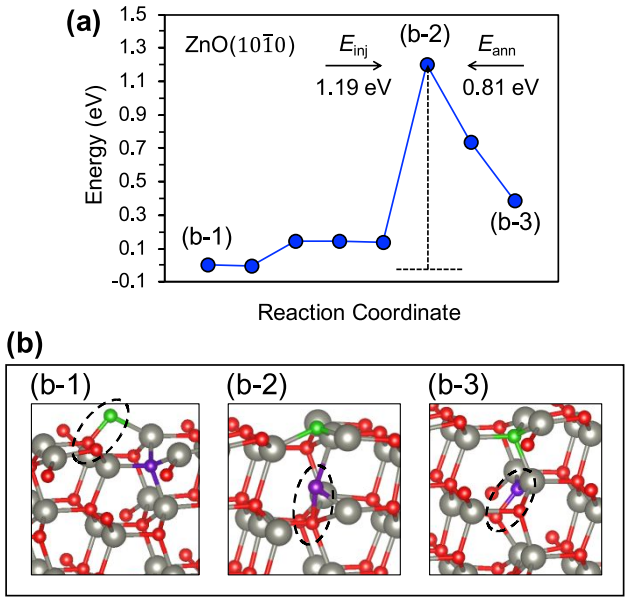

Figure 3. (a) Activation barrier diagram with (b) corresponding geometries at key points along the reaction coordinate for interchange between O adsorbed on the ZnO(10$\bar{1}$0) surface and resident in the first layer under the surface. Rightward movement along the reaction coordinate corresponds to the injection process; leftward corresponds to annihilation. For convenience, key geometries corresponding to initial (b-1), transition (b-2) and final (b-3) states are referenced to an injection process rather than to annihilation. Red and gray spheres respectively designate oxygen and zinc lattice atoms. Green and purple spheres designate key participating O atoms.

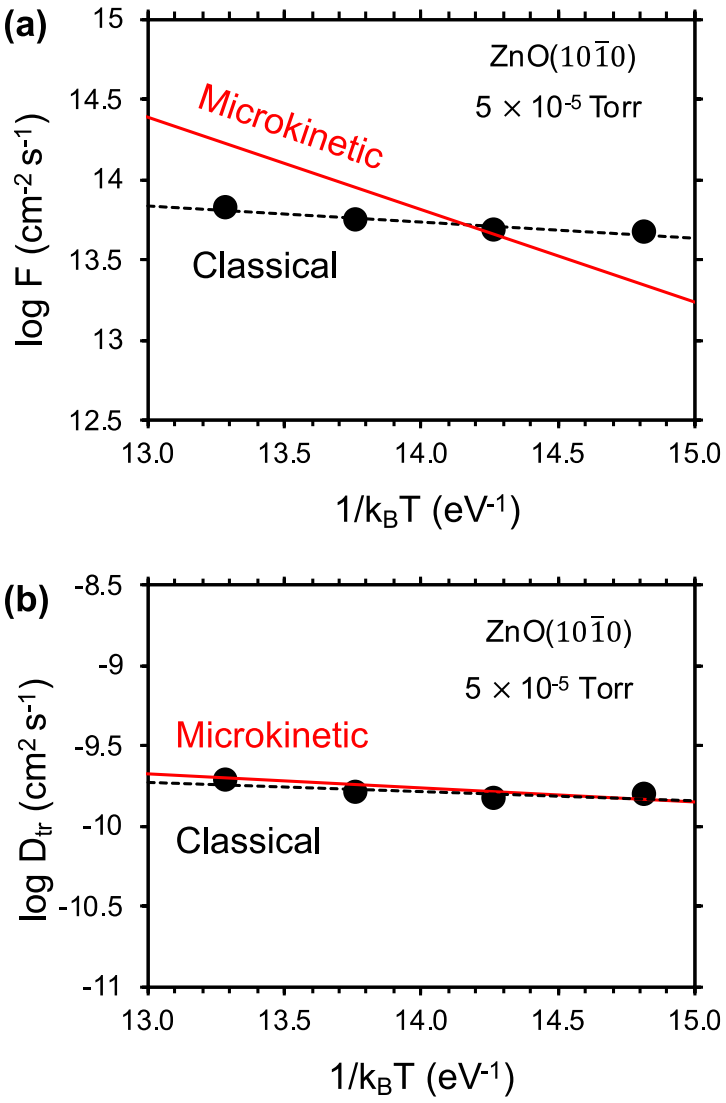

Figure 4. Arrhenius plots of (a) net injection flux F and (b) effective diffusivity D_{tr} for classical thermodynamic and microkinetic models at P_{O_2}= 5 × 10^{-5} Torr.

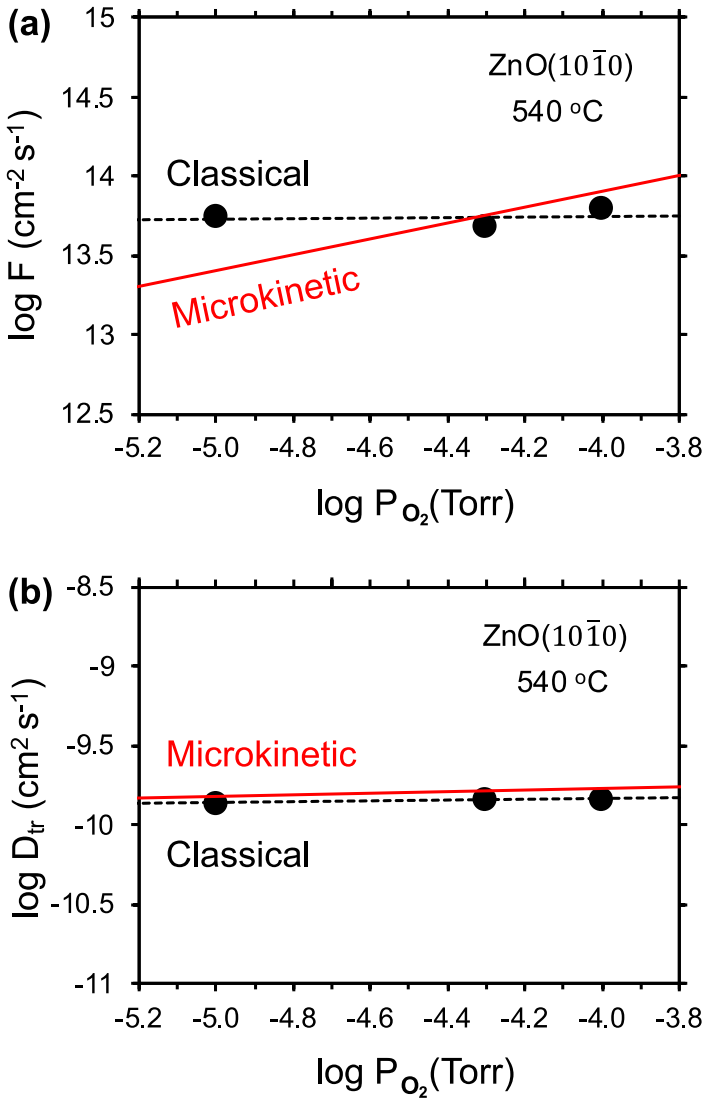

Figure 5. Oxygen partial pressure dependence of (a) net injection flux F and (b) effective diffusivity D_{tr} for analytical and microkinetic models at T = 540 °C.

Tables

Table 1. Components of composite parameters F and D_{tr} for O_i computed by the classical thermodynamic and microkinetic models Activation energy is given in eV. The units for pre-exponential factors of F and D_{tr} are $cm^{-2}\ s^{-1}$ and $cm^2\ s^{-1}$, respectively.

Parameter	Activation energy at $P_{O_2} = 5 \times 10^{-5}$ Torr		Pre-exponential factor at $P_{O_2} = 5 \times 10^{-5}$ Torr		Exponent b in $P_{O_2}^b$ at 540 °C	
	classical	microkinetic	classical	microkinetic	classical	microkinetic
F	0.23 ± 0.05	1.32 ± 0.01	$1 \times 10^{(15.17 \pm 0.35)}$	$1 \times 10^{(21.88 \pm 0.01)}$	0.02 ± 0.09	0.5
D_{tr}	0.13 ± 0.07	0.13 ± 0.01	$1 \times 10^{(-9.01 \pm 0.45)}$	$1 \times 10^{(-9.01 \pm 0.01)}$	0.03 ± 0.01	0.05

Table 2. Initial and final microkinetic parameters for O_i.

Parameter	Definition	Initial value	Final estimate
ΔH_f	enthalpy of O_i formation	3.4 eV	0.44 ± 0.05 eV
ΔS_f	entropy of O_i formation	4.5 k_B	7.7 ± 0.7 k_B
ΔH_{fs}	effective formation enthalpy for sequestration sites	1.0 eV	1.2 ± 0.12 eV
S_{tot}	effective formation prefactor for sequestration sites	1.0×10^{25} cm^{-3}	$(2.13 \pm 0.2) \times 10^{30}$ cm^{-3}
c	effective pressure exponent in $(P_{O_2}/P^0)^c$ for sequestration sites	0.1	0.45
E_{hop}	hopping barrier of bulk O_i	0.5 eV	0.89 ± 0.08 eV
$D_{0,hop}$	hopping prefactor of bulk O_i	4.0×10^{-2} $cm^2\ s^{-1}$	$(3.25 \pm 0.32) \times 10^{-3}$ $cm^2\ s^{-1}$
E_{diss}	barrier to liberate O_i from bulk defect complexes	2.2 eV	1.6 ± 0.1 eV
A_{diss}	prefactor to liberate O_i from bulk defect complexes	1.0×10^{13} s^{-1}	$(1.0 \pm 0.1) \times 10^{13}$ s^{-1}
E_{inj}	injection barrier	1.5 eV	1.0 ± 0.1 eV
ν_{inj}	injection prefactor	1.0×10^{13} s^{-1}	$(1.0 \pm 0.1) \times 10^{13}$ s^{-1}
n_{sat}	saturation concentration of injection sites	3.2×10^{13} cm^{-2}	$(1.68 \pm 0.1) \times 10^{14}$ cm^{-2}
S_0	zero-coverage annihilation probability of O_i	6.5×10^{-5}	$(4.5 \pm 0.4) \times 10^{-7}$